

Influence of sputtering power on the properties of thin layers of GZO for photovoltaic applications

H. Mahdhi · Z. Ben Ayadi · J. L. Gauffier ·
K. Djessas · S. Alaya

Received: 12 November 2014 / Accepted: 12 February 2015 / Published online: 19 February 2015
© Springer Science+Business Media New York 2015

Abstract In the present work, we have deposited gallium doped zinc oxide thin films by magnetron sputtering technique based nanocrystalline particles elaborated by sol–gel method. In the first step, the nanoparticles were synthesized by sol–gel method using supercritical drying in ethyl alcohol. The structural studied by X-ray diffractometry indicates that GZO has a polycrystalline hexagonal wurzite structure with a grain size of about 30 nm. Transmission electron microscopy measurements have shown that very small particles of GZO are present in the aerogel powder. Then, thin films were deposited onto glass substrates by rf-magnetron sputtering at ambient temperature. The influence of RF sputtering power on structural, morphological, electrical, and optical properties were investigated. It has been found that all of the films deposited were polycrystalline with a hexagonal wurtzite structure and preferentially oriented in the (002) crystallographic direction. The film deposited at 60 W showed the lowest electrical resistivity of $3.5 \times 10^{-3} \Omega \text{ cm}$ achieved through the highest Hall mobility of $9.30 \text{ cm}^2 \text{ V}^{-1} \text{ s}^{-1}$. All the GZO films in this study showed the optical transmittances higher than 80 %.

1 Introduction

In recent years, much effort has been invested in zinc oxide (ZnO) for different applications. In fact, ZnO exhibits many significant characteristics due to its direct gap of 3.37 eV at room temperature (RT), high free-exciton binding energy of about 60 meV, and excellent optical properties. ZnO is a very promising II–VI semiconductor for optoelectronic; applications in the UV region, especially for piezoelectric transducers [1], the optical waveguides, acousto-optic, other photo-electronic devices [2] and transparent electrodes [3, 4]. Doped ZnO materials have been extensively studied, because of their remarkable optical and electrical properties. The mechanisms of doping may be deviating from the stoichiometry of ZnO, mainly by the introduction of excess zinc atoms in interstitial position, or by the creation of oxygen vacancies (the centers created then behave as electron donors) [5], or by substituting zinc atoms or oxygen atoms by foreign network different valence. The addition of Group III metal dopants, such as Al, In and Ga, increases the electrical conductivity and transparency of ZnO films. The incorporation of these elements into the ZnO lattice can stabilize the film, at high temperatures, and increase its electrical conductivity [6]. Among these elements, Ga is the most effective n-type dopant in ZnO since the ionic and the covalent radii (0.62 and 1.26 Å) are more close to those of Zn (0.74 and 1.31 Å) and the covalent bond length of Ga–O (1.92 Å) is also closely matched with that of Zn–O (1.97 Å) [7, 8].

The GZO thin films can be prepared by a variety of methods such as evaporation [9], Chemical vapour deposition (CVD) [10, 11], spray pyrolysis [12], magnetron sputtering [13–15], and sol–gel technique [16] and pulsed laser deposition (PLD) [17]. However, among these techniques, sputtering and sol–gel processes offered much

H. Mahdhi (✉) · Z. B. Ayadi · S. Alaya
Laboratoire de Physique des Matériaux et des Nanomatériaux
appliquée à l'Environnement, Faculté des Sciences de Gabès,
Cité Erriadh Manara Zrig, 6072 Gabès, Tunisie
e-mail: hayetmahdhi@yahoo.fr

J. L. Gauffier
Département de Physique, INSA de Toulouse, 135 Avenue de
Rangueil, 31077 Toulouse Cedex 4, France

K. Djessas
Laboratoire Procédés, Matériaux et Energie Solaire (PROMES-
CNRS), Université de Perpignan, Rambla de la
thermodynamique, Tecnosud, 66100 Perpignan Cedex, France

more advantages. Sputtering performs high deposition rate, with no toxic gas emissions, is easy to expand to large scale glass substrates with no undesired layer formation problems [18], and is low cost and simple method. On the other hand, sol–gel technique emerged within the last two decades and quickly became one of the most important and promising new material fabrication methods. Indeed, besides the fact that it is a low cost technique, it enables researchers to easily design and fabricate a wide variety of different materials, including the possibility of doping even at high level concentrations at RT. Compared with other techniques, the sol–gel method have many advantages such as low cost, simple synthesis equipment, easy fabrication of large-area, easier adjustment of composition, being able to carry out doping at molecular level. Especially, are suitable for the fabrication of oxide nanoparticles [19]. How to prepare high-quality ZnO nanoparticles by sol–gel method has become a researches subject for a comparison between the structural and optical properties of nanocrystalline ZnO nanoparticles such as crystallite size and band gap energy.

In our previously research, we developed a novel method to fabricate ZnO film as-deposited from ZnO nanostructures synthesized by sol–gel technique [20]. Therefore, the structural properties of obtained ZnO thin-films were dependent on the ZnO nanoparticles. Furthermore, the properties of as-deposited ZnO films were partly depended on the properties of substrates, such as the crystal orientation, the conductivity, as well as the roughness. In this paper, high-quality GZO transparent conductive films are prepared by rf-magnetron sputtering from aerogel nanopowders, and their structural, electrical and optical properties are investigated as a function of their preparation conditions.

2 Experimental details

In the first step, a nanocrystalline GZO aerogel was prepared by dissolving 20 g of zinc acetate dehydrate $[\text{Zn}(\text{CH}_3\text{COO})_2 \cdot 2\text{H}_2\text{O}]$ as a precursor in 140 ml of methanol. After 15 min under magnetic stirring at RT, an adequate quantity of gallium nitrate $[\text{GaN}_3\text{O}_9]$ corresponding to $[\text{Ga}]/[\text{Zn}]$ ratios of 0.03 was added. After 20 min under magnetic stirring, the solution was placed in an autoclave and dried in the supercritical conditions of ethyl alcohol ($T_c = 243\text{ }^\circ\text{C}$, $P_c = 63.6\text{ bars}$).

In the second step, GZO transparent conductive thin films were deposited on glass substrates by using 13.56 MHz rf-magnetron sputtering. Films with thicknesses of approximately 300 nm were deposited. The sputtering chamber was evacuated to a base pressure of 10^{-5} mbar before introducing the sputtering argon gas with 99.9999 % purity without oxygen. The sputtering targets were prepared from the aerogel powders of GZO. During

the sputtering process, the target-to substrate distance was fixed at 75 mm, the substrate temperature was set at ambient temperature and the rf power is varied from 40 to 100 Watt. The substrates are glass plates of 1 mm thick (soda lime glass), previously cleaned ultrasonically cleaned in HCl, rinsed thoroughly with deionized water and then with alcohol and rinsed a second time. A heat treatment in an oven for a few minutes to remove any residual traces that have escaped prior chemical cleaning.

The structural, morphological, electrical and optical properties were studied in this work. The crystal structure was characterized by X-ray diffraction (XRD) using $\text{CoK}\alpha$ radiation (1.78901 Å). The crystallite size was calculated from XRD data using Scherrer's formula. The GZO nanoparticles were also characterized by transmission electron microscopy (TEM) using JEM-200CX. The composition studies were performed by energy dispersive X-ray spectroscopy (EDX) using a scanning electron microscope JEOL JSM 5410 type with a probe. Surface morphology and roughness were measured using atomic force microscopy (AFM, Topo Metrix). Electrical resistivity, Hall mobility and carrier concentration were measured at RT by a Hall measurement system with the Van der Pauw method. Finally the optical transmittance of the films was determined using a Shimadzu UV-3101 PC spectrophotometer in the wavelength range from 200 to 3000 nm.

3 Results and discussion

3.1 Structural properties of the GZO aerogel nanopowder

Figure 1 shows the XRD spectrum of ZnO nanoparticles doped gallium an adequate quantity of gallium corresponding

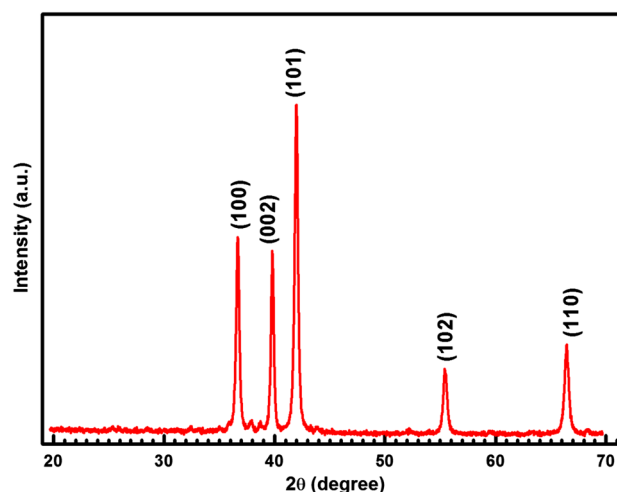


Fig. 1 Spectra of X-ray diffraction of the nanoparticles GZO 3 %

to [Ga]/[Zn] ratios of 0.03 was added. Three pronounced ZnO diffraction peaks (100), (002) and (101) appear at $2\theta = 31.84^\circ$, 34.49° and 36.35° respectively, which are very close to wurtzite ZnO ones [21]. This result indicates that GZO aerogel powder has a polycrystalline hexagonal wurtzite structure. Diffraction lines of ZnO were broad, and diffraction broadening was found to be dependent on Miller indices of the corresponding sets of crystal planes. For our samples, the (002) diffraction line was narrower than the (101) line, which is in turn broader than the (100) line. This indicated an asymmetry in the crystallite shape. It was

supposed that crystallites were in the form of cylinder (prism), having the height (direction of the crystal c -axis) bigger than the basal diameter (crystal axes, a and b). The average grain size was calculated using Scherrer's formula [22]:

$$G = \frac{0.9\lambda}{B \cos \theta_B} \quad (1)$$

where λ is the X-ray wavelength (1.78901 \AA), θ_B is the maximum of the Bragg diffraction peak (in radians) and B is the full width at half maximum (FWHM) of the XRD

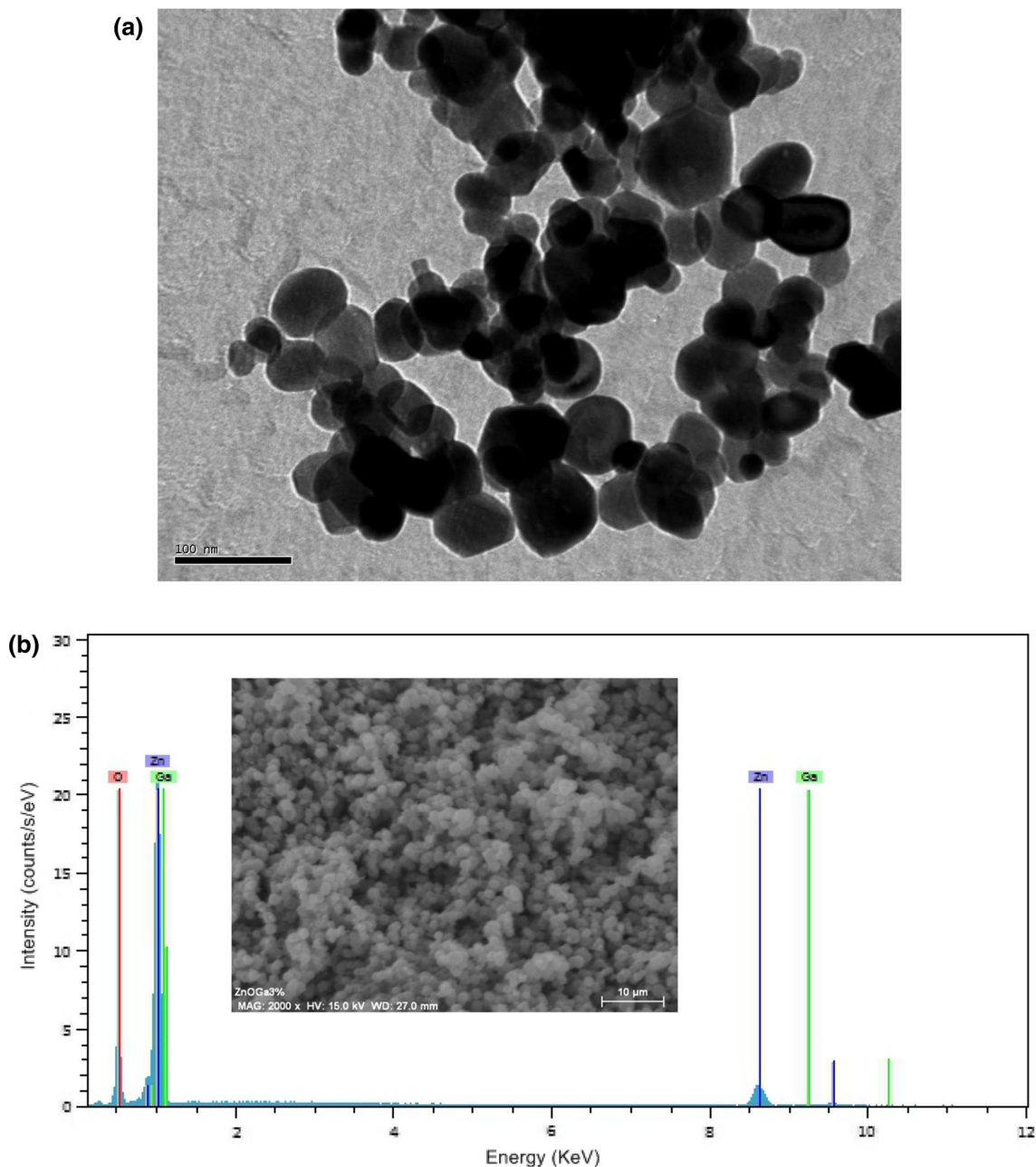


Fig. 2 Typical TEM photograph **a** and SEM showing **b** the general morphology of GZO aerogel nanoparticles

Table 1 Atomic compositions of GZO nanoparticles

Chemical composition in at.%		
Zn	O	Ga
47.12	51.54	1.34

peak. The average grain size of the basal diameter of the cylinder-shape crystallites varies from 14 to 20 nm, whereas the height of the crystallites varies from 25 to 34 nm. These results are in a good agreement with those obtained by K. Omri et al. [19].

TEM measurements (Fig. 2a) show that smaller particles are present in the powder. As seen in the TEM images, the majority of GZO particles present in this powder have a size between 20 and 30 nm. The estimated values, obtained using TEM photograph, are in close agreement with those obtained from the XRD data.

The EDX analysis shown in is shown in Fig. 2b and Table 1 confirmed the presence of gallium in the matrix of ZnO and absence of other impurities. From these analyses, we can conclude that the GZO nanoparticles are homogeneous and quasi-stoichiometric.

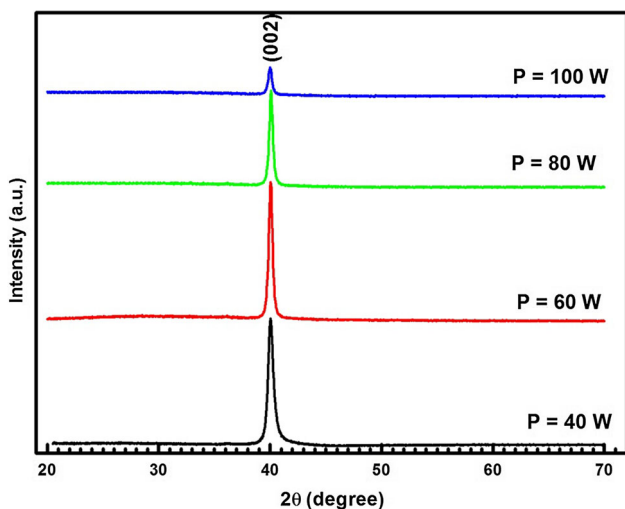


Fig. 3 XRD patterns of GZO thin films with different rf powers

3.2 Structural characterization of GZO films

We report in Fig. 3 the XRD patterns of GZO thin films deposited on glass substrates at different rf power values. All films have hexagonal wurtzite structure. A prominent (002) peak indicates that the crystallite structure of the films is oriented with their c-axis perpendicular to the substrate plane [23]. The films are developed without any second phase, indicating that they have a high quality crystalline structure. It is also clearly observed that, the intensity of the (002) XRD peak increases with increasing rf power.

On the other hand, the variation of the peak location (002) as a function of rf power was observed in Table 2. A small detour in (002) peak was observed when the rf power was varied indicating that some residual stresses within the film may exist [24]. By comparing the curves, we see that the rf power of more than 40 W, not only the strong diffraction peak (002) is observed, but also the value of the FWHM of the peak (002) indicating that the GZO thin film quality is improved. This behavior is accompanied by an increase in the average crystallite size (see Table 2). Furthermore, this result can be explained by the increase of the energy of the sputtered atoms, which allows the growth of larger grains with increasing power deposition [25], because a number of atoms are sputtered from the target and gets a higher energy that contributes to the film growth. The average crystallite size for these samples was about 18–31 nm estimated from the XRD spectrum by using Scherrer formula [22]. These results indicate that crystallinity is improved at an appropriate sputtering power. The diffraction peak angles of the ZnO thin films were estimated in Table 2, and the lattice parameter c for this film was calculated from XRD patterns by using the following equation [26]:

$$d_{hkl} = \left(\frac{4h^2 + hk + k^2}{3a^2} + \frac{l^2}{c^2} \right)^{-1/2} \tag{2}$$

where a and c are the lattice parameters, h, k and l are the Miller indices of the planes and d_{hkl} is the interplanar spacing. The variations of lattice parameters are shown in Table 2.

Table 2 Variation of the (002) peak positions, FWHM, grain size, interreticular distance (d) lattice constant (c) and the stress (σ) of the films GZO at different sputtering power

Rf-power (Watt)	(002) 2θ (°)	β (°)	G (nm)	d_{hkl} (nm)	c (nm)	σ (GPa)
40	39.99	0.537	18.25	0.2615	0.5230	8.53
60	40.04	0.337	29.20	0.2613	0.5226	6.02
80	40.02	0.333	29.55	0.2614	0.5228	4.80
100	39.98	0.313	31.38	0.2616	0.5232	5.42

The lattice parameters are rf power dependant. This gives rise to a mismatch between the substrate and the deposited thin films. The variation of the interreticular distance d (Table 2), shows that for all the sputtered thin films, the d values are larger than that of ZnO powder which is equal to 0.2603 nm. Thus, we can conclude that all the films exhibit compressive stresses.

Stress of thin films is a very important parameter for the practical application. The total stress in thin films

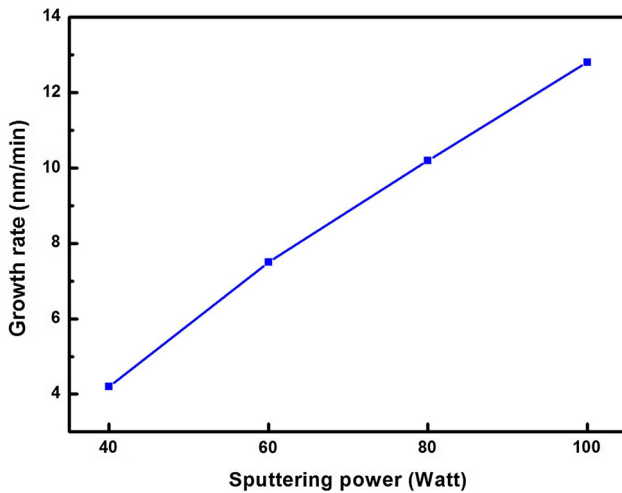


Fig. 4 Growth rate of GZO films as a function of sputtering power

commonly consists of two components. One is the intrinsic stress introduced by impurities, defects and lattice distortions in the crystal, and the other is the extrinsic stress introduced by the lattice mismatch and thermal expansion coefficient mismatch between the film and substrate [27].

$$\varepsilon_z = \frac{c - c_0}{c_0} \times 100 \% \quad (3)$$

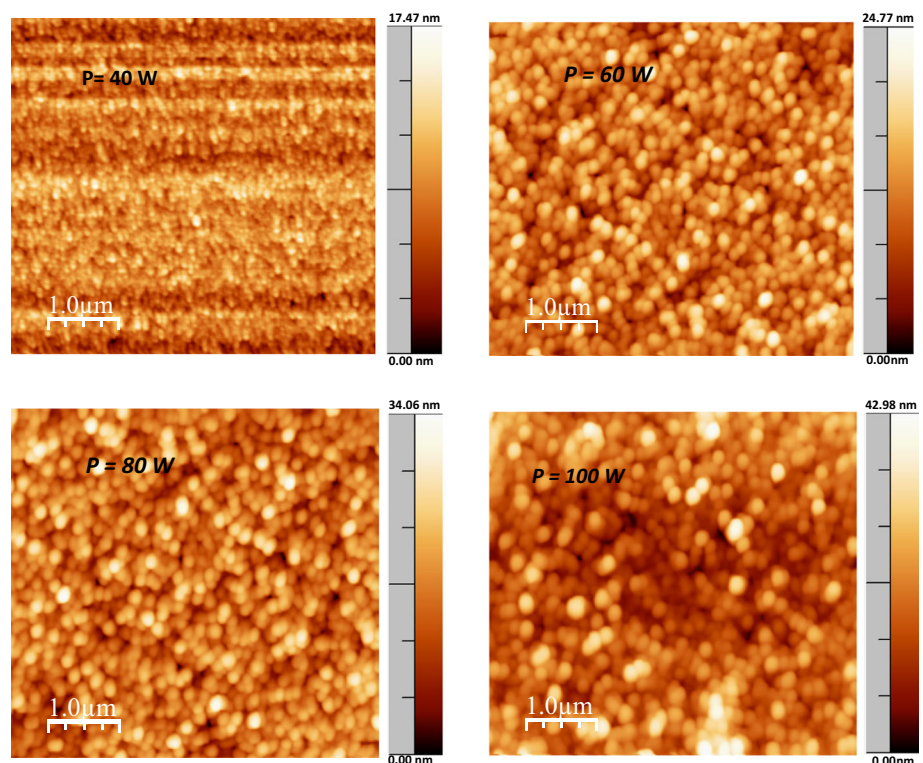
where c is the lattice parameter of the ZnO film calculated from (002) peak of XRD pattern and the c_0 is the lattice parameter for the ZnO bulk ($c_0 = 0.52065$ nm). The stress in the plane of the films was calculated based on the biaxial strain model, using the following formula [28]:

$$\sigma = \frac{2C_{13}^2 - C_{33}(C_{11} - C_{12})}{C_{13}} \cdot \varepsilon_z \quad (4)$$

where $C_{11} = 209.7$ GPa, $C_{12} = 121.1$ GPa, $C_{13} = 105.1$ GPa, and $C_{33} = 210.9$ GPa are the elastic stiffness constant of bulk ZnO. The estimated values of stress σ in the films grown at different sputtering power are listed in Table 2. The total stress in the film commonly consists of two components. One is the intrinsic stress introduced by impurities, defects and lattice distortions in the crystal, and the other is the extrinsic stress introduced by the lattice mismatch and thermal expansion coefficient mismatch between the film and substrate.

Figure 4 shows the dependence of the growth rate on the sputtering power. It is observed that a clear increase in

Fig. 5 2D AFM micrographs ($5 \mu\text{m} \times 5 \mu\text{m}$) for the ZnO:Ga films with different sputtering powers



growth rate as sputtering power increase. The Growth rate and the sputtering power is basically a linear relationship. This increase indicates that the number of atoms sputtered from the target is proportional to the sputtering power [29]. When the sputtering power increase from 40 to 100 W, the growth rate increase from 4.20 to 12.80 nm/min.

The sputtering power dependence of crystallinity and crystallite sizes for GZO films was also revealed by their AFM micrographs. Figure 5 show the surface morphologies of the GZO samples deposited at sputtering power values of 40, 60, 80 and 100 W, respectively. From the figure, we can observe that the crystallite sizes increase on elevating the sputtering power because the ions or ion clusters can obtain more energy prior to collision with the substrates. The RMS surface rough nesses were about 3.6, 9.25, 10.20 and 10.80 nm. This also means that the crystallite sizes were increased with elevating the sputtering power. These results are consistent with the XRD observation.

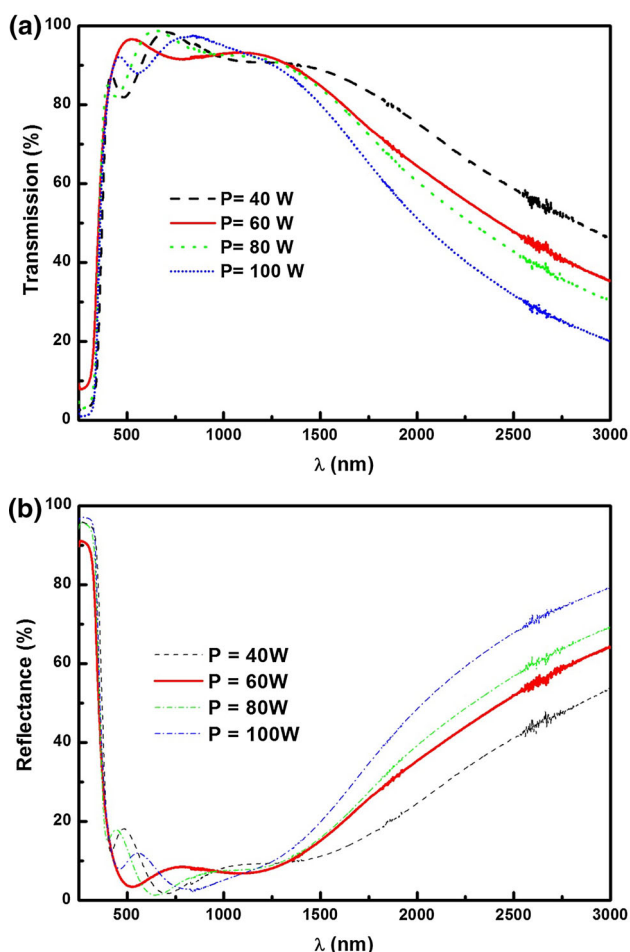


Fig. 6 Transmittance and reflectance spectra of GZO films deposited at various rf powers

3.3 Optical properties of GZO thin films

The transmission spectra and the reflection spectra of GZO thin films deposited by rf magnetron sputtering to deposit different power are shown in Fig. 6. All spectra show a high transparency in the visible range with a good transmission of the order of 90 % and exhibit a low reflection (<20 %). The steep drop of the transmission for the lower wavelengths at 320 nm, corresponding to absorption in GZO due to the transition between the valence band and the conduction band. This area is used to determine the energy of the optical gap.

The transmission coefficient decreases $\lambda > 1000$ nm, this decrease is due to absorption by free carriers (electrons in the case of ZnO:Ga is n-type) which takes place at the plasma frequency.

The optical absorption coefficient (α) is calculated from the transmittance data where the reflection losses are taken into consideration, by [30]:

$$\alpha = \frac{1}{d} \text{Ln} \frac{\sqrt{(1 - R)^4 + 4T^2R^2} - (1 - R)^2}{2TR^2} \tag{5}$$

where d is the thickness of the film and R and T are the reflection and the transmission respectively.

In the direct transition semiconductor, the optical absorption coefficient (α) and the optical energy band gap (E_g) are related by [31]:

$$\alpha(h\nu) = C(h\nu - E_g)^{1/2} \tag{6}$$

where C is a constant for direct transition, and $h\nu$ is the energy of the incident photon.

The optical band gap E_g of the films can be obtained by plotting $(\alpha h\nu)^2$ versus $(h\nu)$ and extrapolating the linear portion of this plot to the energy axis as shown in Fig. 7. We see that the band gap of GZO films increases with

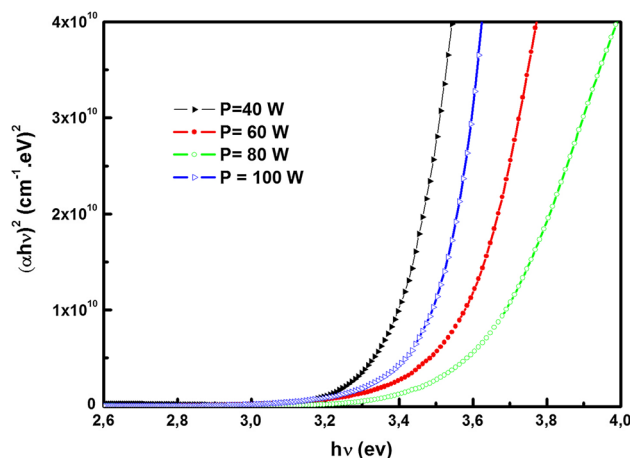


Fig. 7 Plots of $(\alpha h\nu)^2$ versus photon energy ($h\nu$) of GZO thin films with various rf powers

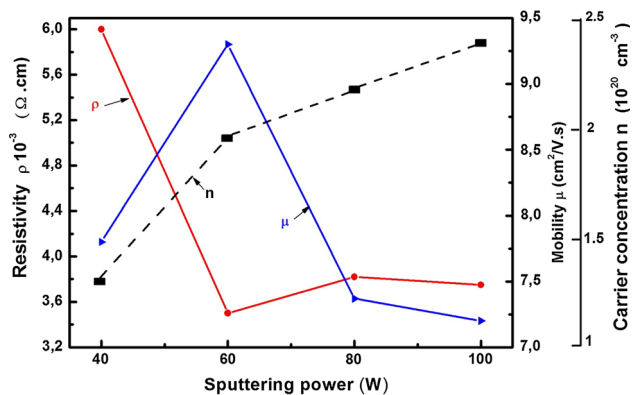


Fig. 8 Resistivities, mobility and carrier concentration of GZO thin films as a function of sputtering power

increasing rf power from 3.38 to 3.64 eV (Fig. 7). All the values are larger than that of pure ZnO (3.30 eV). With increase in sputtering power, the value of E_g increases. The increase in the optical gap for ZnO doped layers is mainly due to the phenomenon of band filling known as the Burstein-Moss effect [32, 33], which increases the gap (blue shift) with increasing the concentration of charge carriers.

3.4 Electrical properties of GZO films

The variation of the resistivity (ρ), carrier concentration (n) and mobility (μ) of GZO films with rf power are shown in Fig. 8. It is clear that the increase in power deposition from 40 to 100 W causes a decrease in resistivity up to 60 W, and then decreases with further increase of sputtering power. The minimum electrical resistivity is obtained for a power of 60 W deposits, the lower the value of ρ is about $3.5 \cdot 10^{-3} \Omega \cdot \text{cm}$, this is due to both increase in the mobility around $9.30 \text{ cm}^2 \text{ V}^{-1} \text{ s}^{-1}$ and carrier concentration to $1.92 \cdot 10^{20} \text{ cm}^{-3}$. As we previously reported, the grain size increases with the power deposition and subsequent grain boundaries decrease. Therefore increasing the mobility of charge carriers is attributed to the decrease of scattering centers which causes a decrease of the electrical resistivity. In addition, the decrease of the resistivity is due to the increase in the charge carrier concentration (n) from donors Ga^{3+} incorporated in the interstitial or substitutional sites of Zn^{2+} [34, 35]. However, above the sputtering power of 60 W, the resistivity began to slightly increase as a result of the decrease of mobility. The improvement of conductivity was contributed to better crystallinity of GZO film and its dense microstructure with larger grain sizes as seen from the XRD results. Thereby, the carrier concentration and mobility can be increased because of the decrease of impurity scattering and grain boundary scattering. From this study, we conclude that the value of 60 W is the optimal power deposition in our work.

4 Conclusion

In summary, high-quality transparent conductive GZO films were grown on glass substrates at RT by rf-magnetron sputtering process using aerogel nano powders prepared by sol-gel technique. The effect of rf power on the structural, electrical and optical properties of GZO thin films deposited in the experiment was investigated. All of the obtained films were polycrystalline with the hexagonal structure and had a preferred orientation with c-axis perpendicular to the substrate. Highly transparent films with a visible transmittance higher than 90 % and a minimum resistivity of $3.5 \cdot 10^{-3} \Omega \cdot \text{cm}$ were obtained by applying rf power at 60 W. Therefore, it is clear that GZO thin films deposited by rf-magnetron sputtering at RT can be used in optoelectronic devices such as transparent conducting electrodes in LCDs and solar cells.

References

1. A.E. Jiménez, J.A. Soto Urueta, *Sol. Energy Mater. Sol. Cells* **52**, 345–353 (1998)
2. Y.R. Rye, T.S. Lee, J.A. Lubguban, H.W. White, Y.S. Park, C.J. Youn, *Appl. Phys. Lett.* **87**, 153504 (2005)
3. A. Maldonado, M.L. Olvera, S. Terado-Guerra, R. Asomoza, *Sol. Energy Mater. Sol. Cells* **82**, 75 (2004)
4. M. Girtan, M. Socol, B. Pattier, M. Sylla, A. Stanculescu, *Thin Solid Films* **519**, 573 (2010)
5. K.Y. Cheong, N. Muti, S.R. Ramanan, *Thin Solid Films* **410**, 142–146 (2002)
6. H. Gomez, M. de la, L. Olvera, *Mater. Sci. Eng.* **134**, 20 (2006)
7. B.T. Lee, T.H. Kim, S.H. Jeong, *J. Phys. D Appl. Phys.* **39**, 957 (2006)
8. G.K. Paul, S.K. Sen, *Mater. Lett.* **57**, 742 (2002)
9. T. Minami, S. Ida, T. Miyata, Y. Minamino, *Thin Solid Films* **445**, 268 (2003)
10. B.M. Ataev, A.M. Bagamadova, A.M. Djabrailov, V.V. Mamedov, R.A. Rabadanov, *Thin Solid Films* **260**, 19 (1995)
11. J. Hu, R.G. Gordon, *J. Appl. Phys.* **72**, 5381 (1992)
12. M. De La, L. Olvera, A. Maldonado, R. Asomoza, *J. Mater. Sci. Mater. Electron.* **11**, 383 (2000)
13. S.N. Bai, T.Y. Tseng, *J. Mater. Sci. Mater. Electron.* **20**, 253 (2009)
14. M. Miyazaki, K. Sato, A. Mitsui, H. Nishimura, *J. Non Cryst. Solids* **218**, 323 (1997)
15. F. Jia, Q. Wang, D.L. Zhu, S. Han, P.J. Cao, W.J. Liu, Y.X. Zeng, Y.M. Lu, *J. Mater. Sci. Mater. Electron.* **25**, 2934 (2014)
16. S.N. Bai, S.C. Wu, *J. Mater. Sci. Mater. Electron.* **22**, 339 (2011)
17. S.M. Park, T. Ikegami, K. Ebihara, *Thin Solid Films* **513**, 90 (2006)
18. G. Aygun, I. Yildiz, *J. Appl. Phys.* **106**, 014312 (2009)
19. K. Omri, I. Najeh, R. Dhahri, J. El Ghoul, L. El Mir, *Microelectron. Eng.* **128**, 53 (2014)
20. Z.B. Ayadi, L. El Mir, K. Djessas, S. Alaya, *Nanotechnology* **18**, 445702 (2007)
21. Y. Chem, D.M. Bagnall, H.K. Koh, K.T. Park, K. Hiraga, Z.Q. Zhu, T. Yao, *J. Appl. Phys.* **84**, 3912 (1998)
22. B.D. Cullity, *Elements of X-ray Diffraction* (Addison-Wesley, Reading, 1978), p. 102

23. Y. Chem, D.M. Bagnall, H.K. Koh, K.T. Park, K. Hiraga, Z.Q. Zhu, T. Yao, *J. Appl. Phys.* **84**, 3912 (1998)
24. E.M. Bachari, G. Baud, S.B. Amor, M. Jacquet, *Thin Solid Films* **348**, 165 (1999)
25. R.C. Chang, S.Y. Chu, C.S. Hung, Y.T. Chung, *Surf. Coat. Technol.* **200**, 3235 (2006)
26. G.J. Fang, D.J. Li, B.L. Yao, *Phys. Status Solidi A* **193**, 139 (2002)
27. H.C. Ong, A.X.E. Zhu, G.T. Du, *Appl. Phys. Lett.* **80**, 941 (2002)
28. Y.G. Wang, S.P. Lau, H.W. Lee, S.F. Yu, B.K. Tay, X.H. Zhang, K.Y. Tse, H.H. Hng, *J. Appl. Phys.* **94**, 1597 (2003)
29. M.K. Puchert, P.Y. Timbrell, R.N. Lamb, *J. Vac. Sci. Technol. A* **14**, 2220–2230 (1996)
30. D.K. Schroder, *Semiconductor Material and Device Characterization* (Wiley, New York, 1990)
31. J.I. Pankove, *Optical Processes in Semiconductors* (Dover, New York, 1976)
32. E. Burstein, *Phys. Rev.* **93**, 632 (1954)
33. T.S. Moss, *Phys. Soc. Lond. B* **67**, 775 (1954)
34. K. Ellmer, G. Vollweiler, *Thin Solid Films* **496**, 104 (2006)
35. Y. Igasaki, H. Saito, *J. Appl. Phys.* **69**, 2190 (1991)